CHEMISTRY OF MATERIALS

ARTICLE

pubs.acs.org/cm

Structural Key of the Thermal Expansion and the Oxide Ionic Conduction in Derivatives of $La_2Mo_2O_9$: a Temperature-Controlled Neutron Diffraction Study of β-$La_{1.7}Bi_{0.3}Mo_2O_9$

Gwenaël Corbel,*[,†] Emmanuelle Suard,[‡] and Philippe Lacorre[†]

[†]Laboratoire des Oxydes et Fluorures, UMR-6010 CNRS, Université du Maine, Avenue Olivier Messiaen, 72085 Le Mans Cedex 9, France

[‡]Institut Laue-Langevin, BP 156, 38042 Grenoble Cedex 9, France

Supporting Information

ABSTRACT: A thorough temperature-controlled powder neutron diffraction study was carried out on a Bi-substituted LAMOX (derivatives of $La_2Mo_2O_9$) oxide ion conductor β-$La_{1.7}Bi_{0.3}Mo_2O_9$. It allowed us to identify the subtle structural distortions at the origin of, or correlated to, the peculiarities of the ionic conduction process, which were misinterpreted in previous studies on related compounds. The main distortions concern the morphology of the anti-tetrahedral building units of the cationic framework hosting conducting anions, rather than the tilt/rotation of such units as previously postulated. An analysis of the ionic displacements and the temperature factors within these $[O1(La,Bi)_3Mo]$ units upon heating suggests that the successive expansions of $[(La,Bi)_3]$ and $[(La,Bi)_2Mo]$ triangular faces enables some O1 oxide ions to escape from their initial position toward partially occupied O2 and O3 sites, respectively. The increase of ionic conductivity/mobility observed above about 450 °C and ascribed to a transition toward a Vogel−Tammann−Fulcher (VTF)-type assisted transport regime would consequently be due to the opening up of new conduction paths rather than to an intrinsic increase in mobility of O2 and O3 ions on their low temperature conduction paths.

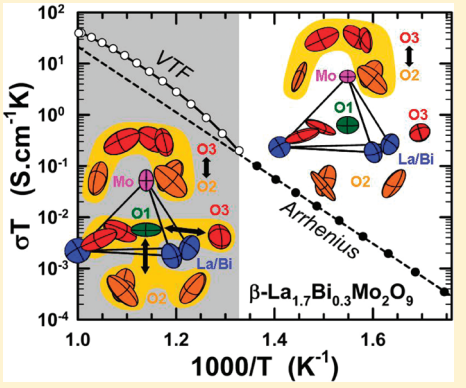

KEYWORDS: lanthanum molybdate, LAMOX, thermal expansion, anti-structure, bismuth, lone pair, neutron powder diffraction, oxide ion conduction, Vogel−Tammann−Fulcher law

0. INTRODUCTION

Fast oxide ion conductors are of considerable interest for a range of environmentally friendly applications including Solid Oxide Fuel Cells (SOFC), oxygen sensors, and oxygen separation membranes. In 2000, Goutenoire et al. discovered a novel oxide ion conductor $La_2Mo_2O_9$.[1,2] This binary oxide exhibits, above a reversible α (monoclinic) → β (cubic) structural phase transition at 580 °C, an anionic conductivity (6.10^{-2} S cm^{-1} at 800 °C) higher than that of cubic 8 mol %Yttria Stabilized Zirconia (YSZ8%), the conventional SOFC electrolyte. Thus, the strategy was to stabilize the high-T anionically disordered cubic β-form to lower temperatures through solid solution formation to enhance the oxide ion conductivity below the first order transition. Numerous works were then devoted to aliovalently or isovalently substituted derivatives of $La_2Mo_2O_9$, the so-called LAMOX family.[3] A prerequisite to integrate promising cubic derivatives of $La_2Mo_2O_9$ as core materials in any electrochemical devices is their thermal stability in the operating temperature range 300−700 °C. Our recent investigations along this line showed that the β form of several K^+ (4−6 mol %[4]), Ca^{2+} (3−4 mol %[5,6]), Ba^{2+}(7.5−10 mol %[4]), Nd^{3+} (20−60 mol %[7]), Eu^{3+} (7.5−10 mol %[8]) substituted LAMOX can be retained in a metastable state at room temperature through a relatively low cooling rate of 5 °C/min. In neodymium and europium series, the metastability is topological in nature (successive β-metastable/α and α/β transitions in the temperature range 460−500 °C and at around 570 °C, respectively), while transient exsolution of β-$KLaMo_2O_8$, $CaMoO_4$, and $BaMoO_4$ Scheelite-type phases above ≈500 °C is inherent to aliovalent substitutions. In the latter situation, the depletion originates from a compositional metastability of the solid solution, supersaturated in aliovalent solute at high temperature. Both instabilities are somewhat reminiscent of what is observed in oxides with high concentration of point defects such as aliovalently substituted zirconias.[9,10]

In thermodynamically stable β-LAMOX however, the evolution of conductivity upon heating exhibits, above 400−450 °C, a deviation from a conventional Arrhenius-type behavior in concordance with an increase of cell volume compared to its linear expansion at lower temperature.[8,11] Above 450 °C, the conductivity curve can be satisfactorily fitted with a Vogel−Tammann−Fulcher (VTF) model.[12−14] In such a VTF-type model, the oxide ion migration is assumed to be thermally assisted by the host matrix distortion/vibration. Recently, we have proposed a non

Received: November 12, 2010
Revised: January 12, 2011
Published: February 08, 2011

conventional description of the β-$La_2Mo_2O_9$ structural arrangement based on [O1La_3Mo] anti-tetrahedra.[15] The [O1LaMo] framework, built up from these elementary units sharing each of their three La corners, delineates tunnels inside which are located disordered O2 and O3 atoms. A plausible explanation for the regime of framework assisted-transport above 450 °C was proposed from a geometric analysis of the possible flexibility of this cationic sublattice in the $P2_13$ space group of β-$La_2Mo_2O_9$,[11] assuming a non-distortive thermal expansion of [O1La_3Mo] anti-tetrahedral elementary building units,[15] and their rotation at high temperature. A convenient way to quantify this rotation is to define the tilt angle δ of the anti-tetrahedron around the 3-fold axis of the structure (or around its [O1−Mo] direction) from the interatomic distance d_{La-La} and the cubic cell parameter a, according to the formula: $\tan \delta = -[8/3 \times (d_{La-La}/a)^2 - 1]^{1/2}$. While keeping the overall cubic symmetry, it was shown that the weak increase of the tilt angle δ (or decrease of its absolute value $|\delta|$) could expand the structure above 400−450 °C by opening up the framework's tunnels, thus favoring migration of O2 and O3 ions.

Neutron diffraction remains especially suited for the crystal structure analysis of oxides thanks to the high neutron scattering factor of oxygen, which allows its accurate positioning in the structure. In that way, Tealdi et al.[16] have recently undertaken to detect such a subtle structural distortion in 5 mol %K-LAMOX ($La_{1.9}K_{0.1}Mo_2O_{8.9}$) by temperature-controlled neutron diffraction. These authors have shown that the absolute value of tilt angle $|\delta|$ increases with increasing temperature in the range 400−700 °C. This surprising evolution, opposite to the one calculated from our geometric analysis, means that the rotations of [O1(La,K)$_3$Mo] units in 5 mol %K-LAMOX would close down tunnels, contrary to what these authors claimed in their paper. As mentioned above, the K series is unfortunately liable, for content higher than 4 mol %K, to β-$KLaMo_2O_8$ demixing phenomenon above ≈500 °C with a lowering in K content of the LAMOX phase.[4] Thereby, one can wonder whether the structural study of Tealdi et al. on β-$La_{1.9}K_{0.1}Mo_2O_{8.9}$ really reflects intrinsic structural behavior of the high temperature β form with increasing temperature: is it due to the growing instability of the metastable phase in the range 500−1000 °C or to the incidence on the structure of a substitute K, larger in size than La?

A raw powder sample of $La_{1.7}Bi_{0.3}Mo_2O_9$ derivative exhibits a stabilization of the β form in a large temperature range up to 950 °C, as demonstrated in the current paper thanks to thermal analysis and temperature-controlled diffraction. The first aim of the current structural analysis, undertaken by temperature-controlled neutron diffraction, was to check if the suspected closing down of tunnels takes place upon heating in the stable β-$La_{1.7}Bi_{0.3}Mo_2O_9$ phase. The second aim was to gain better insight into the flexibility of the β-$La_2Mo_2O_9$ structure by partially substituting trivalent lanthanum by trivalent bismuth in the framework. Indeed, the outer electrons of Bi^{3+} ion form an electronic $6s^2$ lone-pair, the presence of which in the framework is likely to either distort the structure in a larger magnitude than potassium does in $La_{1.9}K_{0.1}Mo_2O_{8.9}$ or to restrict the rotations of anti-tetrahedra. The careful examination of the temperature incidence on the geometry and tilts/rotations of [O1(La/Bi)$_3$Mo] elementary building units has allowed us to reveal the structural key of the expansion mechanism and of the oxide ion conduction in β-$La_{1.7}Bi_{0.3}Mo_2O_9$.

1. EXPERIMENTAL DETAILS

1.1. Synthesis and Purity of Raw Powder Sample. One gram of polycrystalline sample of β-$La_{1.7}Bi_{0.3}Mo_2O_9$ was prepared by conventional solid state reaction from elementary oxides La_2O_3 (REacton 99.9% from Alfa Aesar), Bi_2O_3 (ReagentPlus 99.9% from Sigma-Aldrich) and MoO_3 (PURATREM 99.999% from Strem Chemicals). Prior to use, La_2O_3 was calcinated in air for 12 h at 1000 °C to remove adsorbed water and carbon dioxide. Attempts to obtain a pure single phase from the stoichiometric mixture heated in air at 500 and 900 °C (heating and cooling rates of 2 °C/min with grindings in between) failed. Total weight losses less than 1 wt % were systematically noted and X-ray diffraction pattern collected after completion showed a single impurity peak at $2\theta(\text{CuK}\alpha) = 27.5°$ in addition to diffraction lines of a major β-$La_2Mo_2O_9$-type phase. Furthermore, no improvement was achieved by lowering the temperature down to 800 °C. Note that the total weight loss and the amount of this secondary phase grow as the annealing temperature increases from 800 to 1000 °C. Since the synthesis of pure $La_2Mo_2O_9$ is currently performed in the above conditions, the formation of the secondary phase was presumably ascribed to the volatility of bismuth oxide at high temperature (melting point of Bi_2O_3 = 817 °C[17]). Different excesses of Bi_2O_3 (2.5, 5, 7.5 mol %) were therefore used to balance for any bismuth deficiency in the synthesis of $La_{1.7}Bi_{0.3}Mo_2O_9$ at 900 °C. However, a continuous increase in intensity of the impurity reflection at $2\theta(\text{CuK}\alpha) = 27.5°$, correlated with the appearance of three additional peaks located in the scattering angle 31−32.5°, was observed with the increase of Bi_2O_3 excess. These four peaks showing a good match with L-$Bi_6Mo_2O_{15}$ (PDF No. 56-1473[18]), the single peak observed on the diffraction pattern of the sample prepared without an excess of Bi_2O_3 was ascribed to this bismuth molybdate. The formation of such a minor phase with a Mo/Bi ratio smaller than unity could originate from a weak loss of MoO_3 (melting point = 801 °C[17]), taking place at a temperature higher than 800 °C, on account of its incomplete reaction with bismuth and lanthanum oxides at lower temperatures. Finally, as shown in Supporting Information, Figure S1, a pure single β-phase is obtained with an excess of 0.75 mol % MoO_3 and no excess of Bi_2O_3 (Above 1 mol % MoO_3 in excess, a monoclinic $La_2(MoO_4)_3$-type phase crystallized (PDF No. 70-1382 [18])). The above process was performed 10 times to get the 10 g of sample used in the neutron diffraction study.

1.2. Neutron Diffraction. A constant wavelength (1.593641 Å) neutron powder diffractogram was recorded in static air from the high resolution two-axis diffractometer super-D2B of Institut Laue-Langevin (Grenoble, France). For data collection at room temperature, the 10 g sample of β-$La_{1.7}Bi_{0.3}Mo_2O_9$ was loaded in a cylindrical vanadium can (∅14 mm). For data collection above room temperature, the powder sample was transferred to a cylindrical silica glass container open to air to avoid the bismuth/molybdenum reduction upon heating. Temperature-controlled neutron diffractograms were collected at 100 °C intervals between 100 and 900 °C using the same diffractometer equipped with a standard ILL furnace. Data were collected at and above room temperature in the [−7.45° to 162°] range for approximately 2 h at each temperature with a 0.05° step. The program FullProf[19] was used for Rietveld refinements. The line-shape was modeled by a standard pseudo-Voigt function using a Caglioti Full Width at Half Maximum (FWHM)-type function (refined parameters U, V, W, η) with a J.-F. Bérar and G. Baldinozzi profile asymmetry correction below a scattering angle of 40° (in 2θ)[20] (2 first adjustable parameters). The neutron diffraction pattern collected at room temperature, in a regular cylindrical vanadium container, shows a modulated background at scattering angles higher than 30° in 2θ (Figure 2). These undulations arise from short-range correlation of atomic positions O2 and O3 with fractional occupancies in β-$La_2Mo_2O_9$-type structure.[15,21,22] The pair correlation distance deduced from the Debye function ($d = 2\pi \times 1.23/Q$) is around 2.8 Å which is in good agreement with typical O−O interatomic distance. This contribution of the elastic diffuse scattering coming from a local static oxygen disorder is common in fast ionic conductors such as cubic 22−26 mol %Y[23] and 15 mol %Ca[24] stabilized zirconias and $Bi_{26}Mo_{10}O_{69}$.[25] In addition to this intrinsic modulation, neutron diffraction patterns collected in a cylindrical vitreous silica container in the temperature range 100−900 °C exhibit three parasitic broad peaks of the vitreous silica container at Q-wave vector positions 1.5, 2.9, and 5.25 $Å^{-1}$.[26] Then, the wavy background intensity was estimated from

linear interpolation between up to 85 points manually selected in regions free from Bragg reflections of space group $P2_13$ (No. 198). The Diamond software[27] was used to draw the crystal structure.

1.3. Differential Thermal Analysis. The differential Thermal Analysis (DTA) thermogram was collected on a ~94 mg raw powder sample with a TGA/DTA Q600 SDT TA Instruments apparatus (Pt crucibles, α-Al_2O_3 as a reference) under air flow (100 mL/min) in the room temperature (RT) to 800 °C range (heating/cooling rate of 20 °C/min).

1.4. Transport Property. A dense ceramic sample of β-$La_{1.7}Bi_{0.3}Mo_2O_9$ (relative density 98(1)% of theoretical density) was obtained using the method extensively described in ref 8. After sintering in air for 5 h at 875 °C and cooling down at 5 °C/min, the phase purity was checked on the pellet by X-ray diffraction. Thin Pt films electrodes were deposited by RF sputtering on both flat faces of the sintered pellet. Ionic conductivity was measured by using a classical symmetric two-electrodes electrochemical cell connected to a Solartron 1296 dielectric interface and a Solartron 1260 frequency response analyzer. Complex impedance spectra were recorded over the 10 MHz to 0.05 Hz range (alternating current (AC) signal amplitude of 50 mV, 40 points/decade) under dry air flow every 20 °C (35 min thermal equilibration) at increasing temperature from 300 to 720 °C. A typical complex impedance spectrum plotted in the Nyquist complex plane is presented in Supporting Information, Figure S2. Impedance spectra can be satisfactorily least-squares fitted using the Z-view 3.0a software[28] with a series combination of two R//CPE elements (where R is a pure resistance and CPE is a Constant Phase Element). On the basis of the values of capacitance obtained, the first arc ($\approx 7.7.10^{-12}$ to $1.8.10^{-11}$ F) was assigned to the bulk response, while the second one ($\approx 1.8.10^{-6}$ to $2.3.10^{-5}$ F) at the low-frequency side is characteristic of a polarization phenomenon associated with oxide ion conduction between the sample and the platinum electrodes. No evidence of any other contribution associated with grain boundary resistance was detected in the whole impedance spectra recorded at different temperatures.

2. RESULTS AND DISCUSSION

2.1. β-$La_{1.7}Bi_{0.3}Mo_2O_9$: a Stable Cubic Member of the LAMOX Family. As a prerequisite to a deeper structural study of the β-$La_{1.7}Bi_{0.3}Mo_2O_9$ thermal expansion, DTA was carried out to probe the thermal stability of raw powder sample. The DTA thermogram of β-$La_{1.7}Bi_{0.3}Mo_2O_9$ reported in Figure 1a, shows that only one weak and broad endothermic event (peak maximum at 519 °C, onset at 475 °C) was measured in the temperature range RT to 800 °C. As earlier stated for stable cubic isovalently Eu-substituted $La_2Mo_2O_9$ compositions,[8] this DT signal is ascribed to a thermal trace of the change in conduction mechanism from an Arrhenius-type behavior at low temperature to the postulated thermally assisted VTF regime. As demonstrated in Figure 1b, the temperature dependence of the total conductivity of β-$La_{1.7}Bi_{0.3}Mo_2O_9$ in the temperature range 300−460 °C can be satisfactorily fitted with a conventional Arrhenius-type law $\sigma T = \sigma_0 \exp[-E_a/RT]$ with a pre-exponential factor $\log(\sigma_0) = 7.74$ S K cm^{-1} and an activation energy E_a = 1.27 eV (correlation coefficient $r^2 = 0.9999$). When departure from linearity is observed at temperatures higher than 480 °C, the fit with the empirical VTF model $\sigma T = \sigma_0 \exp[-B/R(T - T_0)]$ gives a high correlation coefficient $r^2 = 0.9998$ with a pre-exponential factor $\log(\sigma_0) = 8.85$ S K cm^{-1}, a pseudo-activation energy $B = 0.21$ eV, and a temperature at which oxide ion disordering starts becoming dynamic $T_0 = 246$ °C. Note that, the change in conduction mechanism takes place at around 470 °C which is in good agreement with the onset of the transition determined by DTA at 475 °C. In Figure 2, temperature-controlled neutron diffraction (or X-ray diffractograms in Supporting Information, Figure S1) performed on raw powder gives a further confirmation of the thermal stability of β-$La_{1.7}Bi_{0.3}Mo_2O_9$ in air. As shown in Supporting Information, Figure S1, the thermal evolution of the (231) cubic diffraction peak, the most sensitive to the slight monoclinic distortion of the β-$La_2Mo_2O_9$ form, did not exhibit any peak splitting or broadening (potentially caused by a release of topological metastability, if any, on heating up to 950 °C in air). Le Bail fits of all the X-ray diffraction patterns collected at different temperatures for β-$La_{1.7}Bi_{0.3}Mo_2O_9$ were successfully carried out in the cubic cell and space group $P2_13$ (No. 198) with the program Fullprof. Figure 3 displays the similar evolution against temperature of cubic cell volume determined from Rietveld refinements of neutron diffraction patterns (see details in the next section). Two thermal domains with linear dependences of cubic cell volume are observed corresponding to an increase in Thermal Expansion Coefficient (TEC) above 400 °C. As shown in Figure 1b, this change in TEC concomitantly occurs with the rise of conductivity above 470 °C. Thereby, $La_{1.7}Bi_{0.3}Mo_2O_9$ behaves the same way as stable cubic members of the Eu-substituted $La_2Mo_2O_9$ series.[8]

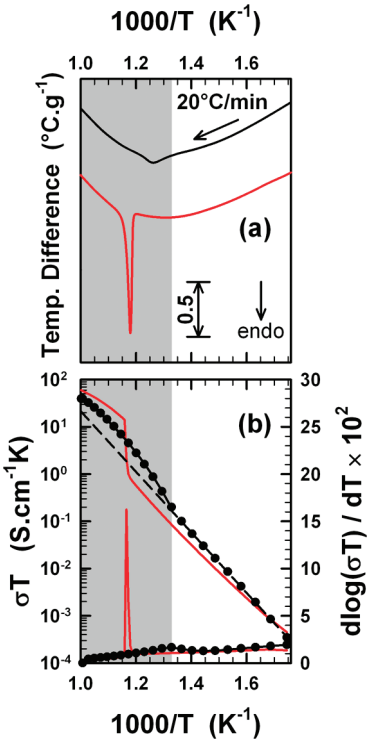

Figure 1. (a) DTA thermograms upon heating in air of raw powder samples showing the structural $\alpha \rightarrow \beta$ phase transition for $La_2Mo_2O_9$ (solid red line) and the thermal trace of the Arrhenius to VTF change in the conduction mechanism for β-$La_{1.7}Bi_{0.3}Mo_2O_9$ (solid black line, Onset at 475 °C, Peak maximum at 519 °C). (b) Temperature dependence of the electrical conductivity of β-$La_{1.7}Bi_{0.3}Mo_2O_9$, fitted with a conventional Arrhenius law in the linear part at low temperature (dashed black line) and with the empirical VTF model when departure from linearity is observed at higher temperature (solid black line). The conductivity curve of $La_2Mo_2O_9$ is added as solid red line for reference (pellet sintered 3 h at 1000 °C, relative density 96(1)% of theoretical density). At the bottom, plot of the first derivative of the conduction with respect to temperature is shown.

dx.doi.org/10.1021/cm103255r |Chem. Mater. 2011, 23, 1288–1298

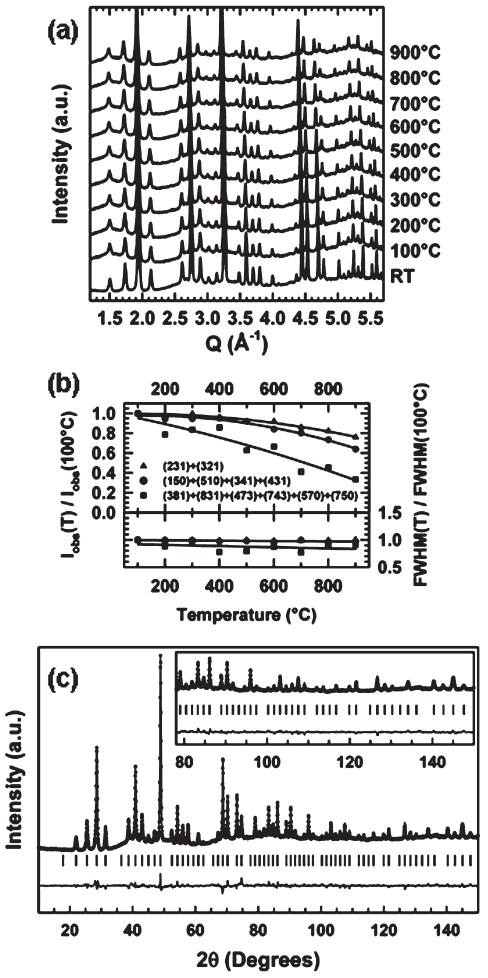

Figure 2. Neutron diffraction patterns of β-$La_{1.7}Bi_{0.3}Mo_2O_9$: (a) modulation of the background showing a first maximum around a Q-wave vector position of 2.75 Å^{-1} ($Q = 4\pi \sin \theta/\lambda$) at room temperature and the parasitic broad peaks of vitreous silica container at 1.5, 2.9, and 5.25 Å^{-1} for patterns collected from 100 to 900 °C (see text for details). (b) Evolution of the relative intensity and the FWHM of selected diffraction peaks as a function of temperature (Single peak fitting with a Pseudo-Voigt function). (c) Observed (dots), calculated (lines), and difference (below) patterns at room temperature using the structural model in Table 1. Vertical markers give Bragg peak positions of space group $P2_13$ (No. 198).

2.2. Rietveld Refinements of Temperature-Controlled Neutron Diffraction Patterns. The crystal structure of β-$La_{1.7}Bi_{0.3}Mo_2O_9$, at room temperature, has been refined from neutron powder diffraction pattern by the Rietveld method using the high-temperature cubic structure of β-$La_2Mo_2O_9$ as a starting structural model.[29] The site occupation factors for La and Bi in special positions 4a were kept fixed to 0.85 and 0.15, respectively, according to nominal Bi content. The occupancy of O3 site was constrained with that of O2 site to fulfill oxygen stoichiometry. θ-zero shift, parameters of the profile shape function, cubic cell parameter a, atomic positions and anisotropic temperature factors were refined step-by-step together (37 refined parameters). Then successively, the structure refined at a lower temperature was used as starting model for refinement of the next higher temperature one. Using this strategy of refinement gives a non-positive definite matrix of atomic displacements β_{ij} for the O3 site, all the more frequent that the temperature is higher than 400 °C.

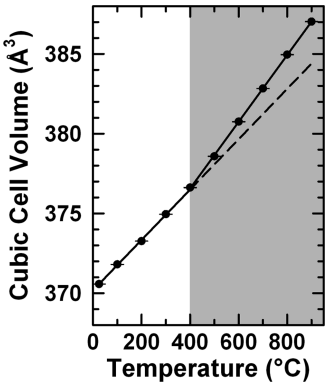

Figure 3. Temperature dependence of cubic cell volume for β-$La_{1.7}Bi_{0.3}Mo_2O_9$ determined from Rietveld refinement of temperature-controlled neutron diffraction data (Table 1). TECs (calculated from linear regression) are 14.2×10^{-6} °C^{-1} and 18.9×10^{-6} °C^{-1} in the temperature range 25−400 °C and 400−900 °C, respectively.

As shown in Figure 2b, increasing the temperature from 100 to 900 °C induces a monotonic reduction in intensity of Bragg peaks while keeping almost constant the FWHM. At high scattering angle (squares in Figure 2b), the peak's intensity decreases, at 900 °C, by two-third of their intensity measured at 100 °C. The unphysical temperature factor found for O3 atom might be partly a consequence of the widely spread distribution of nuclear density around this highly disordered site and points out the inadequate harmonic description of the thermal vibration of this mobile ion. Thereby, the anisotropic temperature factors β_{ij} of O3 site were constrained to that of O2.

Since an excess of 0.75 mol % MoO_3 is necessary to obtain a single phase (see Experimental Details), the occupancy factors of lanthanum, bismuth, and molybdenum sites were refined from data collected at room temperature to detect any loss of Bi or Mo during the synthesis. Site occupancies of 0.87(1), 0.17(1), and 1.02(1) were obtained for La, Bi, and Mo, respectively, with reliability factors R_{wp} = 13.5% and R_{exp} = 11.85%. A fairly good agreement with the chemical composition of β-$La_{1.7}Bi_{0.3}Mo_2O_9$ is found without any change in R-factors when compared to refinement with constrained occupancies (Table 1). The site occupancy factors of both cations were therefore fixed to their nominal contents to lower the number of adjustable parameters for the model. Then, all neutron diffraction patterns were satisfactorily modeled by least-squares fitting the structural model consisting in 10 atomic coordinates, 12 anisotropic thermal factors, O2/O3 fractional site occupancies and the cubic cell parameter a. Figure 2c shows the final observed, calculated, and difference diffraction patterns of β-$La_{1.7}Bi_{0.3}Mo_2O_9$ at room temperature. The values of atomic parameters (positions coordinates, equivalent isotropic temperature factors,[30] and site occupancy factors) together with conventional reliability factors are reported in Table 1 for each temperature of the data collection.

2.3. Crystal Structure at Room Temperature. The value of the cubic cell volume at room temperature for β-$La_{1.7}Bi_{0.3}Mo_2O_9$ (V = 371.635(3) Å^3 deduced from Le Bail's fit of X-ray diffraction pattern) is higher than that of the single monoclinic subcell volume of α-$La_2Mo_2O_9$ (V = 366.05(1) Å^3 from X-ray diffraction data). It is worth mentioning that among substituted LAMOX members, $La_{1.7}Bi_{0.3}Mo_2O_9$ exhibits, at RT, the highest relative variation in cell volume with respect to the parent compound α-$La_2Mo_2O_9$: $[V(La_{1.7}Bi_{0.3}Mo_2O_9)-V(La_2Mo_2O_9)]/V(La_2Mo_2O_9)$ = +1.52%

dx.doi.org/10.1021/cm103255r |*Chem. Mater.* 2011, 23, 1288–1298

Table 1. Results of Rietveld Refinement for β-$La_{1.7}Bi_{0.3}Mo_2O_9$ (Cubic Space Group $P2_13$ (No.198)) from Neutron Powder Diffraction Data[a]

	RT	100 °C	200 °C	300 °C	400 °C	500 °C	600 °C	700 °C	800 °C	900 °C
a (Å)	7.1827(1)	7.1907(1)	7.2001(1)	7.2109(1)	7.2216(2)	7.2341(2)	7.2479(2)	7.2611(2)	7.2745(2)	7.2875(3)
V (Å^3)	370.56(1)	371.80(1)	373.26(1)	374.95(1)	376.62(2)	378.58(2)	380.75(2)	382.83(2)	384.95(2)	387.02(2)
atom	multiplicity and Wyckoff letter	positions coordinates	RT	100 °C	200 °C	300 °C	400 °C	500 °C	600 °C	700 °C	800 °C	900 °C
		x	0.8533(2)	0.8544(3)	0.8534(3)	0.8540(3)	0.8536(3)	0.8518(3)	0.8501(3)	0.8493(4)	0.8479(4)	0.8477(4)
La/Bi	4 a	$B_{eq.}$ (Å^2)[b]	4.4(1)	4.7(1)	5.0(1)	5.1(1)	5.2(1)	6.1(2)	6.8(2)	7.0(2)	7.7(3)	8.1(3)
		occupancy	0.85/0.15	0.85/0.15	0.85/0.15	0.85/0.15	0.85/0.15	0.85/0.15	0.85/0.15	0.85/0.15	0.85/0.15	0.85/0.15
		x	0.1677(4)	0.1681(4)	0.1697(5)	0.1708(5)	0.1707(5)	0.1707(6)	0.1701(6)	0.1703(7)	0.1674(8)	0.1667(9)
Mo	4 a	$B_{eq.}$ (Å^2)[b]	2.58(5)	2.77(6)	2.84(6)	3.03(7)	3.02(6)	3.39(7)	3.45(7)	3.73(7)	4.16(8)	4.6(1)
		occupancy	1	1	1	1	1	1	1	1	1	1
		x	0.3137(4)	0.3165(5)	0.3157(5)	0.3199(5)	0.3179(6)	0.3205(5)	0.3181(6)	0.3195(6)	0.3180(6)	0.3189(7)
O1	4 a	$B_{eq.}$ (Å^2)[b]	4.9(1)	6.1(1)	6.5(2)	7.6(2)	7.3(2)	7.6(2)	7.0(2)	7.6(2)	7.1(2)	8.4(2)
		occupancy	1	1	1	1	1	1	1	1	1	1
		x	0.9870(4)	0.9859(5)	0.9865(5)	0.9855(6)	0.9848(6)	0.9858(7)	0.9854(7)	0.9863(8)	0.9861(9)	0.988(1)
		y	0.1795(8)	0.179(1)	0.177(1)	0.177(1)	0.175(1)	0.174(1)	0.171(1)	0.171(1)	0.173(1)	0.172(1)
O2	12 b	z	0.3407(7)	0.3375(8)	0.3393(8)	0.3358(8)	0.3361(9)	0.336(1)	0.336(1)	0.333(1)	0.336(1)	0.332(1)
		$B_{eq.}$ (Å^2)[b]	7.3(2)	7.6(3)	8.2(3)	8.0(3)	8.6(3)	9.4(3)	9.9(4)	10.0(4)	10.6(4)	10.8(4)
		occupancy	0.869(5)	0.850(6)	0.872(6)	0.845(6)	0.859(7)	0.856(7)	0.885(8)	0.880(9)	0.872(9)	0.843(9)
		x	0.916(1)	0.915(1)	0.912(1)	0.913(1)	0.913(2)	0.915(2)	0.915(2)	0.920(2)	0.925(2)	0.925(2)
		y	0.634(2)	0.638(2)	0.628(2)	0.637(3)	0.629(3)	0.626(3)	0.611(4)	0.611(4)	0.615(4)	0.621(4)
O3	12 b	z	0.553(1)	0.550(1)	0.546(1)	0.547(1)	0.545(1)	0.549(2)	0.544(2)	0.547(2)	0.546(2)	0.553(2)
		$B_{eq.}$ (Å^2)[b]	7.3(2)	7.6(3)	8.2(3)	8.0(3)	8.6(3)	9.4(3)	9.9(4)	10.0(4)	10.6(4)	10.8(4)
		occupancy	0.298(5)	0.317(6)	0.295(6)	0.322(6)	0.308(7)	0.310(7)	0.282(7)	0.286(9)	0.295(9)	0.324(9)
no. of reflections			154	154	154	154	154	154	154	156	156	156
R_{wp} (%)			13.5	14.0	14.3	15.2	15.1	14.8	14.6	15.3	14.9	16.0
R_{exp} (%)			11.86	15.83	15.83	16.24	16.55	17	17.59	18.19	18.84	19.47
χ^2			1.3	0.785	0.819	0.876	0.835	0.753	0.688	0.711	0.628	0.676
R_{Bragg} (%)			7.15	7.8	8.38	9.15	9.32	9.08	9.36	10.1	9.79	10.7

[a] For each temperature, lattice parameters, positions coordinates, equivalent isotropic temperature factors and site occupancy factors are listed as well as R-factors and χ^2-values for the fit. [b] $\mathbf{B}_{eq} = ((4a^2)/3)[\boldsymbol{\beta}_{11} + \boldsymbol{\beta}_{22} + \boldsymbol{\beta}_{33}]$.

(from X-ray diffraction data). The magnitude of the lattice expansion involved by Bi^{3+}/La^{3+} substitution is somewhat unexpected since both trivalent ions have nearly equal ionic radii[31] whatever the coordination number. At reverse, a limited reduction of $\Delta V/V$-($La_2Mo_2O_9$) = −0.67% (from X-ray diffraction data) was found for $La_{1.7}Eu_{0.3}Mo_2O_9$[8] despite the big drop of size between Eu^{3+} and La^{3+} ions (≈−8%).[31] Trivalent bismuth stands apart from rare earth substitutes to La since the outer electrons of this p-block ion form an electronic $6s^2$ lone-pair. Andersson and Åström[32] showed that the spatial extension of a stereochemically active lone pair, whatever the electronic orbital, corresponds roughly to the volume of an oxide anion. In this way, the stereochemical activity of bismuth $6s^2$ lone pairs could explain the significant increase in cell volume by substituting 15 mol % of lanthanum by bismuth in β-$La_2Mo_2O_9$.

As already observed at room temperature in β-$La_2Mo_{2-y}W_yO_9$ series,[15] a reduction in the intensity of the Bragg reflections with increasing the neutron scattering angle, is also noted for Bi-substituted LAMOX sample in Figure 2c, leading to large thermal factors for La/Bi, Mo, and oxygen atoms especially O2/O3 (Table 1). If ellipsoids of thermal vibration are highly anisotropic for O2/O3 oxygen atoms (see CIF file in Supporting Information), the thermal displacements of remaining atoms are more isotropic.

We describe next how the structure expands upon heating.

2.4. Structural Distortion of the [O1(La/Bi)Mo] Host Framework upon Heating. In a previous geometrical analysis of the anti-structural framework of β-$La_2Mo_2O_9$, it has been postulated that above 400 °C, the extra cell volume expansion of cubic LAMOX compounds could originate from the opening up of tunnels through a decrease of the tilt angle $|\delta|$ of $[O1La_3Mo]$ anti-tetrahedral building units around the 3-fold axis of the structure.[11] In this "opening" model, the geometry (interatomic distances) of the anti-tetrahedron was kept constant in the whole temperature range, which was not very realistic. In the present investigation, we have undertaken a comparison between the experimental data of the temperature-controlled neutron diffraction study of β-$La_{1.7}Bi_{0.3}Mo_2O_9$ and a calculation from a more realistic expansion model than the basic "opening" one. In this new model, called "linear+opening", a homothetic and linear expansion of the $[O1(La/Bi)_3Mo]$ anti-tetrahedron upon heating has been introduced in addition to the rotating atomic movements because of a postulated opening of tunnels above 400 °C. All details related to this model are reported in the Supporting Information.

In the anti-structure of β-$La_2Mo_2O_9$, the tunnels can be described as resulting from the three-dimensional (3D) interconnections of small cages built up from seven La corner-sharing $[O1La_3Mo]$ basic units, and hosting partially occupied O2 and O3 crystallographic sites. Such a cage in β-$La_{1.7}Bi_{0.3}Mo_2O_9$ is

dx.doi.org/10.1021/cm103255r |Chem. Mater. 2011, 23, 1288–1298

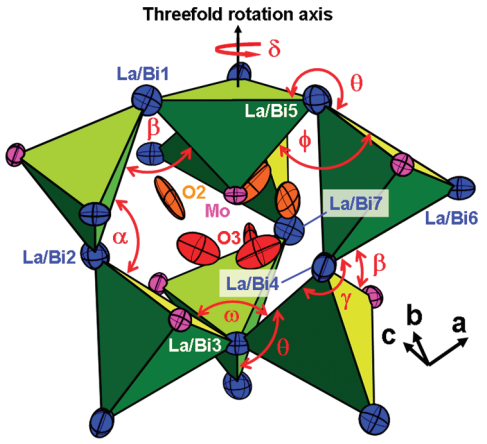

Figure 4. Cage of the 3D cationic framework, built up from seven La/Bi corner-sharing $[O1(La/Bi)_3Mo]$ anti-tetrahedral basic units (green) hosting mobile O2/O3 oxide ions in β-$La_{1.7}Bi_{0.3}Mo_2O_9$. Thermal ellipsoids (at 50% probability) of Mo^{6+} (pink), La^{3+} or Bi^{3+} (blue), O1 (green), O2 (orange), and O3 (red) ion sites determined at room temperature from Rietveld refinement of neutron diffraction data (Table 1).

isolated in Figure 4. One can notice that La/Bi3 atom and the Mo atom close to O2 and O3 sites are located on the same 3-fold axis of the structure. The presence of this symmetry element makes possible a complete description of the cage geometry with the following:

(1) six inter-tetrahedral edge angles between adjacent La/Bi corner-sharing $[O1(La/Bi)_3Mo]$ basic units: α = (La/Bi)1-(La/Bi)2-(La/Bi)3, β = Mo-(La/Bi)1-(La/Bi)2, ω = (La/Bi)2-(La/Bi)3-(La/Bi)4, γ = (La/Bi)3-(La/Bi)4-(La/Bi)6, θ = (La/Bi)1-(La/Bi)5-(La/Bi)6, and ϕ = Mo-(La/Bi)5-(La/Bi)6,

(2) four cation−cation distances: La/Bi1−La/Bi3, La/Bi2−La/Bi4, and Mo−Mo being the three "diagonals" of the cage, while distance Mo−La/Bi3 represents the "bottleneck" of tunnels.

As can be imagined from Figure 4, a change in the tilt angle δ of the anti-tetrahedra as the temperature increases will likely modify the above inter-tetrahedral edge angles and distances within the cage by either closing down or opening up the framework's tunnels.

Let us now determine from our experimental data reported in Table 1 for β-$La_{1.7}Bi_{0.3}Mo_2O_9$, the thermal evolution of all these geometrical parameters. Their temperature dependencies are depicted in Figure 5a. This Figure shows that an almost steady state is observed below 400 °C for the tilt angle $|\delta|$. In absence of change in anti-tetrahedra tilting in the range RT to 400 °C, only linear elongations of interatomic distances are observed without any modification in inter-units angles θ, γ, α, and ω between La/Bi−La/Bi edges. Above 400 °C, the tilt angle $|\delta|$ starts increasing before leveling off at higher temperature. This increase, which in magnitude reaches ≈1.5° over the temperature range 400−900 °C, involves a converse closing of the inter-tetrahedral edge angles γ (≈ −0.5°), θ (≈ −0.8°), ϕ (≈ −1°), β (≈ −1.3°), and ω (≈ −2°). These cooperative rotations of $[O1(La/Bi)_3Mo]$ anti-tetrahedra around their [O1−Mo] direction mainly distort the tunnels along the 3-fold axes of the structure by opening the inter-tetrahedral edge angle α (≈+1.6° in the range 400−900 °C), by increasing the La/Bi1-LaBi3 distance (≈+0.16 Å) and by slightly shortening the La/Bi2-LaBi4 distance (≈−0.03 Å).

To draw a conclusion on the opening up or closing down of the framework's tunnels, the above temperature dependences of

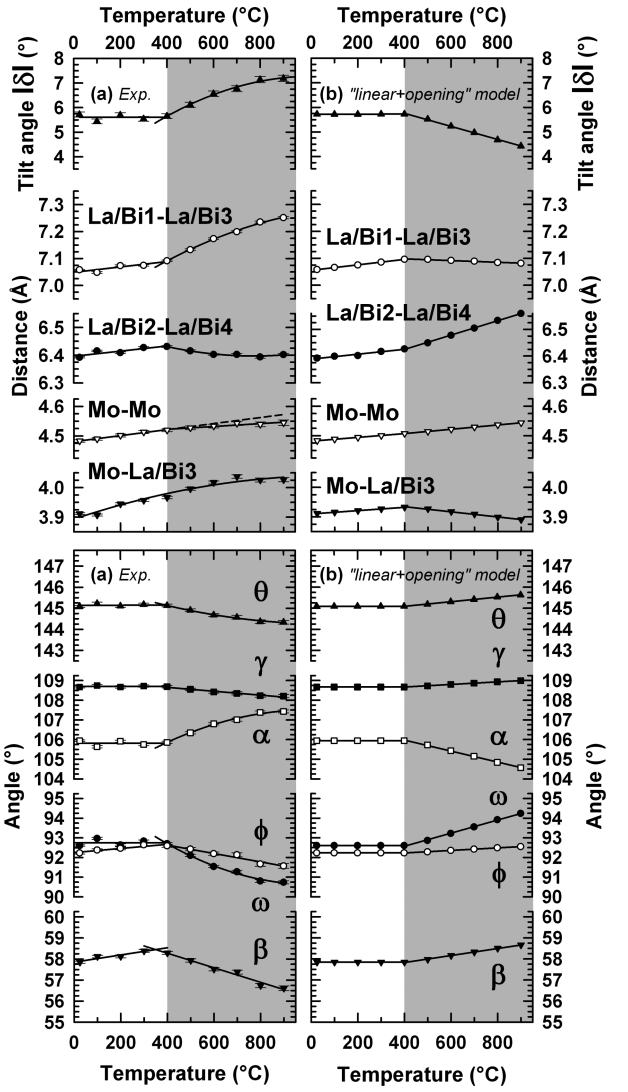

Figure 5. Temperature dependence of cation−cation distances and inter-tetrahedral edge angles within the cage for β-$La_{1.7}Bi_{0.3}Mo_2O_9$: (a) experimental data and (b) data calculated from the "linear + opening" model (see text and Supporting Information). Variations are satisfactorily fitted with quadratic polynomial functions when departure from steady state or linear behavior is observed.

inter-tetrahedral edge angles and cation−cation distances were compared to those obtained from the "linear + opening" model. In Figure 5b, this simulation of a decrease in tilt angle $|\delta|$ above 400 °C, characteristic of an opening up of tunnels with increasing temperature, shows that the way the angles or the distances within the cage change is always opposite to that determined experimentally in β-$La_{1.7}Bi_{0.3}Mo_2O_9$ from neutron diffraction data. This comparison between experiment and simulation demonstrates that the "linear + opening" model of thermal expansion is definitively inadequate and more particularly points out that above 400 °C, the progressive tilt/rotation of $[O1(La/Bi)_3Mo]$ anti-tetrahedra closes the framework's tunnels.

At this stage, one can wonder whether this surprising behavior is specific to cubic bismuth substituted $La_2Mo_2O_9$ or characteristic of all cubic members of the LAMOX family. In their recent structural study performed on β-$La_{1.9}K_{0.1}Mo_2O_{8.9}$[16] air-annealed in the temperature 400−700 °C, Tealdi et al. have mentioned that an

dx.doi.org/10.1021/cm103255r |Chem. Mater. 2011, 23, 1288–1298

opening up of the framework occurs even though the tilt angle $|\delta|$ clearly increases upon heating. This apparent contradiction incited us to determine, from the crystallographic data reported by these authors, the evolutions of inter-tetrahedral edge angles and cation−cation distances as a function of temperature in β-$La_{1.9}K_{0.1}Mo_2O_{8.9}$. Both evolutions are displayed in Supporting Information, Figure S4. It must be noted that in the range 400−700 °C, the rise of anti-tetrahedra tilting for β-$La_{1.9}K_{0.1}Mo_2O_{8.9}$ ($\Delta\delta_{400-700\ °C} = 0.68°$) is of a lesser magnitude than that reported for β-$La_{1.7}Bi_{0.3}Mo_2O_9$ ($\Delta\delta_{400-700\ °C} = 1.11°$), thus softening up the change in edge angles and cation−cation distances observed in the K substituted LAMOX. Nevertheless, Figure S4 shows that angles and distances in β-$La_{1.9}K_{0.1}Mo_2O_{8.9}$ behave roughly the same way as in β-$La_{1.7}Bi_{0.3}Mo_2O_9$ when the tilt angle $|\delta|$ increases in the range 400−700 °C. Contrary to what Tealdi et al. claimed in their paper, a closing down of framework's tunnels also occurs in β-$La_{1.9}K_{0.1}Mo_2O_{8.9}$. Although this thorough structural analysis has been carried out on only two compositions, this behavior is probably representative of all cubic members of the LAMOX family since all these oxides exhibit, with a larger or lower magnitude depending on the substitute, an extra increase in unit cell volume above 400 °C compared to its linear thermal expansion at lower temperature. This consideration points out, however, an obvious contradiction between this increase of TEC above 400 °C and the concomitant closing down of the framework's tunnels. Within our assumption that anti-tetrahedron has an isotropic and linear thermal expansion in the whole temperature range RT to 900 °C, a lowering of TEC above 400 °C would be expected while the structure is closing down. Also to be considered is the singular increase of conductivity observed in LAMOX compounds at high temperature, which is satisfactorily fitted with the empirical VTF equation. Such equation is usually used to model diffusion of mobile ionic species when assisted by thermal expansion and vibration of the host matrix.[33−35] In LAMOX materials, the existence of framework-assisted transport above 400 °C is in question since the closing of the framework's tunnels involved by these rotations cannot make the migration of highly disordered O2 and O3 ions located in these tunnels easier than in the Arrhenius regime at low temperature. Nevertheless, Figure 1b shows no progressive leveling off or decrease of the total conductivity above 400 °C as the tunnels are closing down in β-$La_{1.7}Bi_{0.3}Mo_2O_9$.

Both contradictions incited us to closely look into the temperature incidence on the geometry of the $[O1(La/Bi)_3Mo]$ anti-tetrahedra building up the framework, considering up to now as rigid units. The next section is devoted to such analysis.

2.5. Thermal Expansion of $[O1(La/Bi)_3Mo]$ Anti-tetrahedron. Figure 6a displays the evolution against temperature of the La/Bi−La/Bi and La/Bi−Mo distances within the $[O1(La/Bi)_3Mo]$ basic unit, determined from the experimental data reported in Table 1. Different non linear thermal behaviors of La/Bi−La/Bi and La/Bi−Mo edges are observed. Below and above 400 °C, La/Bi−La/Bi edges undergo two linear regimes of elongation, the rate of lengthening in the range 400−900 °C ($\Delta d_{La/Bi-La/Bi}/\Delta T \approx 10.8 \times 10^{-5}$ Å °C^{-1}) being much larger than at low temperature ($\Delta d_{La/Bi-La/Bi}/\Delta T \approx 6.2 \times 10^{-5}$ Å °C^{-1}). When temperature increases, La/Bi−Mo edges undergo first a linear contraction in length ($\Delta d_{La/Bi-Mo}/\Delta T \approx -5.8 \times 10^{-5}$ Å °C^{-1}) in the range RT to 300 °C before elongating above 300 °C. The unexpected contraction of Mo−La/Bi edges below 300 °C explains why only the angles ϕ = Mo-(La/Bi)5-(La/Bi)6 and β = Mo-(La/Bi)1-(La/Bi)2 between anti-tetrahedral units forming the cage is opening of ≈0.4° − 0.5° in spite of the absence of change in their

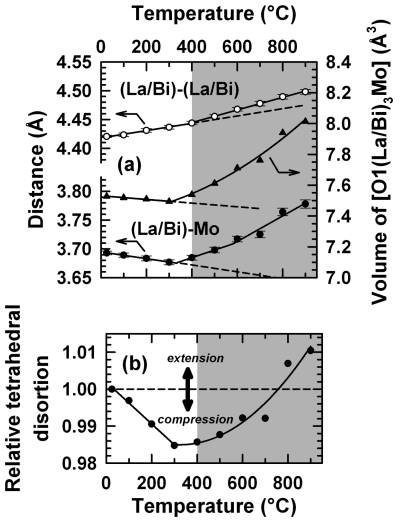

Figure 6. (a) Thermal evolution of La/Bi−La/Bi and La/Bi−Mo edge lengths (Å) and of the volume (Å^3) of the $[O1(La/Bi)_3Mo]$ anti-tetrahedral basic unit in β-$La_{1.7}Bi_{0.3}Mo_2O_9$. (b) Temperature dependence of the tetrahedral relative distortion showing successive thermal compression and extension regimes below and above ≈750 °C, respectively.

tilting (Figures 4 and 5a). In the temperature range 400−900 °C, the elongation of La/Bi−Mo edges is not as regular as that of La/Bi−La/Bi edges. The rate of lengthening of La/Bi−Mo edges, already larger than that of La/Bi−La/Bi edges in the range 400−600 °C, still increases above 600 °C. The elongation of La/Bi−Mo edges in the range 400−900 °C ($\Delta d_{La/Bi-Mo}/\Delta T \approx 18.6 \times 10^{-5}$ Å °C^{-1}) is then nearly twice as large as that of La/Bi−La/Bi edges ($\Delta d_{La/Bi-La/Bi}/\Delta T \approx 10.8 \times 10^{-5}$ Å °C^{-1}). A way to quantify the distortion of the $[O1(La/Bi)_3Mo]$ anti-tetrahedron is to calculate the ratio between its high $h = (d_{La/Bi-Mo}{}^2 - 1/3 \times d_{La/Bi-La/Bi}{}^2)^{1/2}$ and the length of the La/Bi−La/Bi edge ($d_{La/Bi-La/Bi}$). The temperature dependence of the relative distortion of the anti-tetrahedron is given in Figure 6b. It shows that the shortening of La/Bi−Mo edges taking place in the range RT to 300 °C induces a slight compression of the anti-tetrahedron along the [O1−Mo] direction, reaching ≈−1.5% at 300 °C. As the temperature increases from 300 to 900 °C, this compression is canceled by the extra elongation of La/Bi−Mo edges relative to La/Bi−La/Bi edges at ≈750 °C only, above which a true extension of the unit starts. In Figure 6a, the temperature dependence of the volume of the anti-tetrahedron ($V_{anti\text{-}tetrahedron} = \sqrt{3}/12 \times h \times d_{La/Bi-La/Bi}{}^2$) reflects the atypical thermal behavior of La/Bi−Mo edges: first linearly decreases by −0.034 Å^3 in the range RT to 300 °C before increasing of +0.52 Å^3 in the range 300−900 °C.

Let us now examine the incidence of the successive volume contraction and expansion of the anti-tetrahedra and their tilting in the cage on the volumes of the cage and of the tunnels. The volume of the cage can be roughly estimated from the volume of the trigonal bipyramid centered on O3 sites and formed by Mo, La/Bi2, La/Bi3, La/Bi4, and La/Bi7 atoms, as shown in Figure 4 (calculation details in Supporting Information, Figure S5). The relative variation in volume of the tunnels corresponds to the relative variation of the difference between the unit cell volume and the volume of the anti-tetrahedral framework. The volume of the framework is the cumulative volume of the four anti-tetrahedra contained in the unit cell. The relative volume variations of the unit cell, of the framework, of the cage,

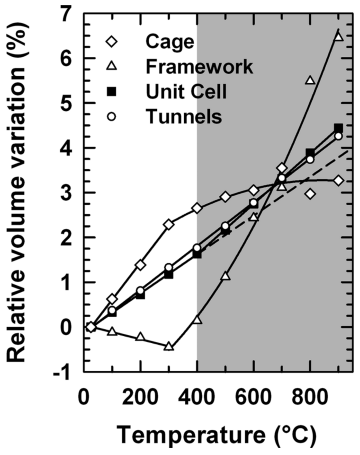

Figure 7. Relative volume variations of the anti-tetrahedral framework, of the cage and of the tunnels compared to that of the cubic unit cell as a function of temperature in β-$La_{1.7}Bi_{0.3}Mo_2O_9$.

and of the tunnels against temperature are displayed in Figure 7. In the range RT to 900 °C, the framework undergoes first a reduction in volume (−0.45%) below 300 °C because of the compression of the anti-tetrahedron along the [O1−Mo] direction (shortening of La/Bi−Mo distances) before expanding above 400 °C. Below 300 °C, this reduction, combined with the elongation of La/Bi1−La/Bi3 and La/Bi2−La/Bi4 distances (Figure 5a), releases space in the surrounding of O3 sites as shown by the rise of the volume of the cage. However, the intercage volume does not expand as much as the cage one since the relative expansion of tunnels (+1.33% at 300 °C) remains lower in magnitude than that of the cage (+2.29% at 300 °C). When the anti-tetrahedron starts increasing in volume and tilting in the cage above 400 °C, the relative volume expansion of the cage decreases in magnitude before leveling off at high temperature. Despite this slowing down of the cage expansion, the volume of tunnels keeps on increasing linearly above 400 °C with the same expansion rate that at low temperature. This increase arises from the extra elongation of the La/Bi1−La/Bi3 distance above 400 °C (+2.25% in the range 400−900 °C, Figure 5a) involved by the concomitant rotations of the anti-tetrahedra and the extra elongation of their La/Bi−La/Bi edges (+1.22% in the range 400−900 °C, Figure 6a). This thorough analysis shows that the increase of TEC of β-$La_{1.7}Bi_{0.3}Mo_2O_9$ above 400 °C (Figure 3) originates from the distortion and the expansion of the anti-tetrahedral framework. Then, the best term describing the complex thermal behavior of the framework is "distortive expansion" rather than "closing down" since the latter term is generally associated to a contraction of volume which is definitively not the case here.

Mo and O1 atoms are both located on the same 3-fold axis of the structure (Figure 4). When the $[(La/Bi)_3Mo]$ anti-tetrahedral surrounding of O1 atom is distorting along this axis upon heating, La/Bi atoms are smoothly moving away from this axis. Then, changes of cation-O1 distances and of tetrahedral angles at O1 central position are expected with increasing the temperature. Their evolutions against temperature are plotted in Figure 8a and Figure S6 in Supporting Information, respectively. Once again, clear non monotonic behaviors are observed. Below ≈400 °C, O1−La/Bi distance slightly decreases, whereas the tetrahedral (La/Bi)−O1−(La/Bi) and Mo−O1−(La/Bi) angles are opening and closing, respectively, with the temperature. As shown in Figure 8b, this deviation results

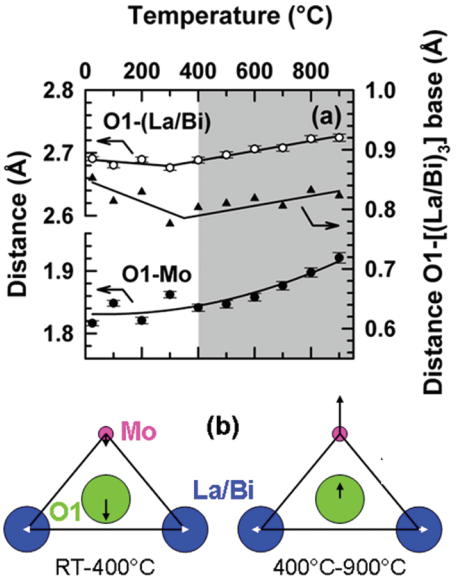

Figure 8. (a) Thermal evolution of O1-cation bond lengths (Å) and of the distance between O1 and the $[(La/Bi)_3]$ base within the $[O1(La/Bi)_3Mo]$ anti-tetrahedral basic unit. (b) Displacements of atoms forming the $[O1(La/Bi)_3Mo]$ anti-tetrahedron between RT and 400 °C (left) and between 400 and 900 °C (right). Arrows lengths are proportional to the displacements (magnified ×10 relative to interatomic distances).

from a displacement of O1 toward the $[(La/Bi)_3]$ base, larger in magnitude than the concomitant displacements of the four vertices arising from the distortion of the anti-tetrahedron. Above ≈400 °C, reverse behaviors are noticed. Mo and O1 atoms move away from the $[(La/Bi)_3]$ base with a displacement Δ of Mo vertex more than twice as large as O1 atom ($\Delta(Mo)_{400-900\,°C} \approx 0.11$ Å, $\Delta(O1)_{400-900\,°C} \approx 0.045$ Å). A significant increase of the O1−Mo distance (Figure 8a) is then observed with the very weak opening of the Mo−O1−(La/Bi) angle (Supporting Information, Figure S6). The unconventional shifts of oxide ion site O1 coupled to the distortion change of its anti-tetrahedral $[(La/Bi)_3Mo]$ environment incited us to consider the possibility for oxygen O1 to escape from this cationic surrounding through the equilateral $[(La/Bi)_3]$ and the isosceles $[(La/Bi)_2Mo]$ triangles toward nearest neighboring vacancies at O2 and O3 sites, respectively.

To determine whether these intersite jumps are geometrically possible, the radius r of the sphere tangent to the three atoms forming a triangular face of the anti-tetrahedron was calculated at each temperature for the two face types $[(La/Bi)_2Mo]$ and $[(La/Bi)_3]$ (see calculation details in Supporting Information, Figure S7). The diameter $2r$ of the sphere in interstitial position within a triangular face can be seen as a rough estimation of the bottleneck through which oxygen O1 should pass to escape from its initial cationic surrounding. In β-$La_2Mo_2O_9$, taking into account the partial occupancy of O2 and O3 sites, the average number of oxygen atoms surrounding La^{3+} and Mo^{6+} are 10 and 4.5, respectively. The coordination number of molybdenum atom being half an integer, the calculation of r for the $[(La/Bi)_2Mo]$ face was carried out with a value of the ionic radius for Mo^{6+} $r_{Mo} = 0.455$ Å, which is the average of ionic radii in four- (0.41 Å) and five- (0.50 Å) fold coordinations tabulated by Shannon.[31] The temperature dependences of r for both $[(La/Bi)_2Mo]$ and $[(La/Bi)_3]$ triangles are shown in Figure 9a. At room temperature, the bottleneck for the equilateral $[(La/Bi)_3]$ triangle is wider than that for the isoceles $[(La/Bi)_2Mo]$ triangle

dx.doi.org/10.1021/cm103255r |*Chem. Mater.* 2011, 23, 1288–1298

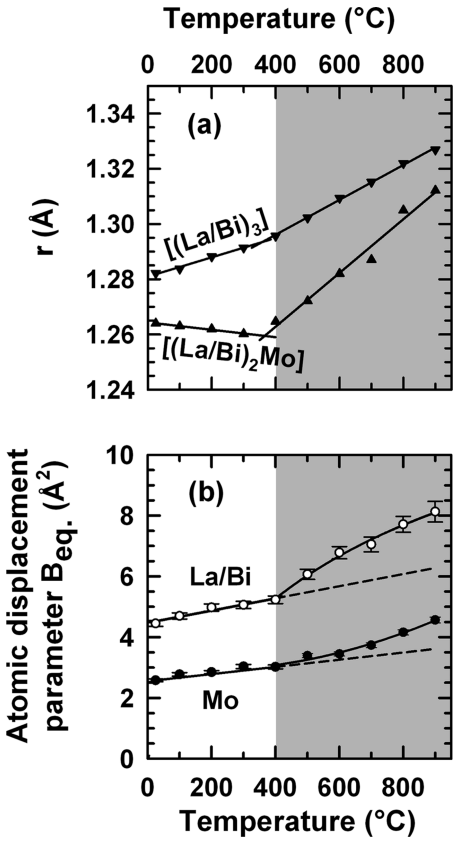

Figure 9. (a) Temperature dependences of equivalent isotropic temperature factors $B_{eq.}$ for La/Bi and Mo atoms in β-$La_{1.7}Bi_{0.3}Mo_2O_9$ showing an extra increase of the thermal vibration above 400 °C relative to the increase observed at lower temperature. (b) Temperature dependences of the radius r of the sphere tangent to the three atoms forming a triangular face of the $[O1(La/Bi)_3Mo]$ anti-tetrahedron.

since La/Bi−La/Bi edges are longer than La/Bi−Mo edges. The contraction in length of La/Bi−Mo edges and the concomitant elongation of La/Bi−La/Bi edges in the range RT to 300 °C increase the difference in size between the two bottlenecks. Above 300 °C, the higher elongation of La/Bi−Mo edges than La/Bi−La/Bi edges widens significantly the bottleneck for the isoceles $[(La/Bi)_2Mo]$ triangle, without however reaching the size of the bottleneck for the equilateral $[(La/Bi)_3]$ triangle. When compared to the ionic radius r_O = 1.36 Å[31] of an oxide ion in triangular coordination, the two bottlenecks remain too narrow for an oxide ion to pass through the faces of the anti-tetrahedron, whatever the temperature. However, it is rather common to observe Mo−O and La−O distances within distorted coordination polyhedra shorter (or longer) than the sum of the ionic radii $r_{Mo} + r_O$ (1.815 Å) and $r_{La} + r_O$ (2.63 Å), respectively. In β-$La_2Mo_4O_{15}$,[36] Mo−O distances as shorter as 1.714(9) Å and 1.712(9) Å were reported for a hexavalent molybdenum in 4-fold and 5-fold coordinations while lanthanum in 10-fold coordination (with an ionic radius for La^{3+} of 1.27 Å[31]) has a very short La−O distance of 2.419(9) Å. Since the $r_{Mo} + r$ and $r_{La} + r$ distances in β-$La_{1.7}Bi_{0.3}Mo_2O_9$ are longer than these shortest Mo−O and La−O distances and increase with the temperature, it seems possible for the O1 ion to escape from its cationic tetrahedral surrounding if a distortion of the triangular bottleneck occurs locally when the oxide ion passes through. In Figure 6a and Figure 9b, one can notice that the stretching of the anti-tetrahedron along its [O1−Mo] direction is

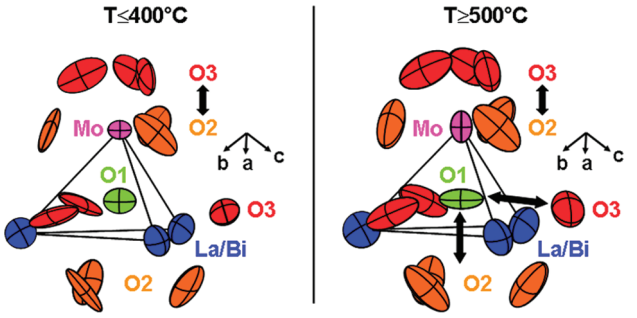

Figure 10. Synoptic scheme of the transition in conduction mechanisms at around 400−500 °C from a low temperature Arrhenius-type regime involving only highly disordered O2/O3 sites located in the framework's tunnels to high temperature regime (VTF-type) in which the distortion/expansion of the anti-tetrahedral $[O1(La/Bi)_3Mo]$ building unit of the framework allows additional intersite O1↔O3 and O1↔O2 jumps to occur. Thermal ellipsoids (at 50% probability) of Mo^{6+} (pink), La^{3+} or Bi^{3+} (blue), O1 (green), O2 (orange), and O3 (red) ion sites were determined at room temperature and at 500 °C from Rietveld refinement of neutron diffraction data (Table 1).

correlated with an extra increase of the thermal vibration for La/Bi and Mo atoms above 400 °C, compared to their linear increase at lower temperature. Whatever the temperature, the oblate spheroid of thermal vibration for La/Bi atom is oriented mostly in a plane orthogonal to the opposite $[(La/Bi)_2Mo]$ face (Figure 10). Between 400 and 500 °C, the prolate spheroid of thermal vibration for Mo atom undergoes a rotation by 90° of its revolution axis to be perpendicular to the opposite $[(La/Bi)_3]$ face of the anti-tetrahedron (Figure 10). Above 400 °C, the Mo atom thus vibrates along the direction orthogonal to the $[(La/Bi)_3]$ base. These spatial orientations of the spheroids of thermal vibrations for La/Bi and Mo atoms and their large vibration amplitudes are consistent with the breathing of bottlenecks favoring O1 ion migration by shortening/elongating $r_{Mo} + r$ and $r_{La} + r$ distances. When only one La/Bi or Mo atom locally is moving from the center of the anti-tetrahedron to outside, an anisotropic opening (or distortion) of three over four bottlenecks existing within the anti-tetrahedron can occur simultaneously. Obviously, the opening of bottlenecks will increase in amplitude with the number of atoms moving at the same time in the same direction (positively correlated motions). The vibration of Mo atom being of much lesser magnitude than La/Bi atom since the temperature is high, the largest and the most isotropic opening in terms of amplitude concerns the bottleneck for the equilateral $[(La/Bi)_3]$ triangle when the thermal motions of its three La/Bi vertices are positively correlated. This bottleneck being also the largest in diameter, it should be much easier for the O1 ion to escape from its cationic surrounding through the $[(La/Bi)_3]$ face than through the $[(La/Bi)_2Mo]$ faces. This conclusion is consistent with dielectric relaxation measurements performed by Wang and Fang on β-$La_{1.85}Bi_{0.15}Mo_2O_9$.[37,38] The temperature dependence of the dielectric loss tan δ exhibits in the temperature range 175−525 °C of two overlapped broad peaks shifting in position toward higher temperature as the frequency increases. These authors have ascribed the most intense relaxation peak and the small shoulder at lower temperature to jumps of O1 oxygen ions toward the nearest-neighboring O3 and O2 sites, respectively. The activation energy relative to O1↔O2 intersites jumps through the $[(La/Bi)_3]$ face (1.2 eV) is lower than that of O1↔O3 jumps through the three remaining $[(La/Bi)_2Mo]$ faces (1.56 eV).

In our structural model used for Rietveld refinements of the neutron diffraction patterns, the O1 site was always considered as

fully occupied whatever the temperature. We have then checked whether this assumption is still valid by refining the occupancy factor of O1, O2, and O3 sites while keeping all structural parameters fixed to values reported in Table 1. To fulfill the oxygen stoichiometry, occupancies of two oxygen sites were in turn constrained and refined. The deficiency of O1 site above 400 °C was found smaller than 1% which does not seem to be in favor of a significant site depletion. The conductivity is a function of mobile carrier concentration and mobility. Then, an increase of the conductivity can originate from an increase of mobile carrier concentration and/or mobility. Because of the absence of a significant increase in deficiency of the O1 site when these oxide ions become mobile above 450 °C, the mobile carrier concentration does not seem to change significantly at the transition. However the above crystallographic study clearly points toward the participation of site O1 to the oxide ions migration process at high temperature. It seems therefore likely that the increase in conductivity originates from the opening up, at high temperature, of new migration paths through the anti-tetrahedral units from and toward O2 and O3 sites (Figure 10). As suggested by the good fit of the conductivity data by a VTF-type model, the abnormal distortive expansion of the cationic surrounding of oxygen site O1 above 400 °C provides further experimental evidence that the cationic framework assists the oxide ion migration through these units, thereby increasing the overall ionic mobility.

2.6. Orientation of the Bismuth $6s^2$ Lone Pair and Effect on Transport Property. The spatial orientation of the bismuth $6s^2$ lone pair in β-$La_{1.7}Bi_{0.3}Mo_2O_9$ might be deduced from the close relationship between structures of β-$La_2Mo_2O_9$ and of β-$SnWO_4$[39] (Lone Pair Substitution concept[40]) and the crystallographic data reported in Table 1. In the structures of β-$La_2Mo_2O_9$ and β-$SnWO_4$ (cubic space group $P2_13$), both Sn^{2+} and La^{3+} ions reside in the same *4a* special position ($\approx 0.85, \approx 0.85, \approx 0.85$). In β-$La_2Mo_2O_9$ (Supporting Information, Figure S8), the oxygen atomic arrangement for La can be described as a stacking along the 3-fold axis of one triangle [3 × O3] and one hexagon [3 × O2 + 3 × O3], at each side of a strongly corrugated hexagon [3 × O1 + 3 × O2] centered on La. In β-$SnWO_4$, the *12b* position, which is partially occupied by O3 ions in β-$La_2Mo_2O_9$, is empty. The stereoactive $5s^2$ lone pair of tin 2+ in β-$SnWO_4$ points along the 3-fold axis toward the triangle formed by the three highly oxygen deficient O3 sites in β-$La_2Mo_2O_9$. Whatever the temperature, the occupancy of the O3 site ($\approx$ 30%) reported in Table 1 for β-$La_{1.7}Bi_{0.3}Mo_2O_9$ is lower than that determined for β-$La_2Mo_2O_9$ at 670 °C ($\approx$ 38%).[29] Substituting partially La^{3+} by the lone pair cation Bi^{3+} in lanthanum molybdate thus would involve oxygen depletion from O3 site at the expense of the O2 site. In that way, this suggests that the bismuth $6s^2$ lone pair is directing toward the center of tunnels and along the migration pathway. Recently, Mohn et al.[41,42] have probed the dynamic of local oxide environment in the anionic conductor δ-Bi_2O_3 by using ab initio molecular dynamic simulations and neutron powder diffraction. It was shown that trivalent bismuth cation in the anionic conductor δ-Bi_2O_3 adopts a highly asymmetric anion surrounding with a stereochemically active lone pair directing toward vacancies. In δ-Bi_2O_3, the flexible Bi−O bonds and O−Bi−O bond angles allow rapid changes in the Bi^{3+} position and its asymmetric coordination shell as the O^{2-} ions migrate, facilitating rapid diffusion. Because of the electrostatic repulsive interaction between oxide ions and lone pairs of electrons, dynamic reorientations of lone pairs necessarily take place during the diffusion thus reducing the energy barriers along migration pathways. As shown in Figure 1, the total conductivity in the VTF regime of β-$La_{1.7}Bi_{0.3}Mo_2O_9$ does not exceed the value reported for β-$La_2Mo_2O_9$. It is noteworthy that the existence of a high electronic contribution hiding a lowering of the anionic conductivity by a blocking effect of the lone pair in β-$La_{1.7}Bi_{0.3}Mo_2O_9$ is ruled out since Marozeau et al.[43] have measured an ionic transference number of ≈0.99 at 700 °C in air by the faradaic efficiency method. If in a similar way to that observed in δ-Bi_2O_3, dynamic reorientation of nonbonding electron pairs on bismuth occurs as oxide ions migrate in β-$La_{1.7}Bi_{0.3}Mo_2O_9$, its benefit impact on the conductivity is limited by the low bismuth content in the molybdate.

3. CONCLUSION

Chemically β-stabilized LAMOX compounds show upon heating a singular rise of oxide ion conductivity above ≈450 °C, correlated with an increase in TEC. The thermal evolution of the conductivity above 450 °C can be satisfactorily fitted by a VTF model, thus suggesting a regime of framework-assisted mobility of oxide ions. In this paper, the crystal structure of β-$La_{1.7}Bi_{0.3}Mo_2O_9$, a stable cubic member of the LAMOX family, was refined from neutron diffraction data at different temperatures in the range RT to 900 °C to highlight the structural key for this close structure/transport relationship. In the anti-structure of β-$La_{1.7}Bi_{0.3}Mo_2O_9$, the tunnels hosting partially occupied O2 and O3 crystallographic sites result from the 3D interconnections of small cages built up from seven La/Bi corner-sharing [O1$(La/Bi)_3$Mo] anti-tetrahedral units. In the temperature range RT to 400 °C, the anti-tetrahedron undergoes an isotropic extension of its [$(La/Bi)_3$] base coupled to a trigonal compression along its non-bridging Mo apex pointing in the cage. This distortion of the basic unit taking place without rotation around the 3-fold axis of the structure, a volume expansion of the cage is observed without any deformation. Above 400 °C, a leveling off of the cage expansion is observed because of a large trigonal extension of the anti-tetrahedron along the non-bridging Mo apex when it tilts in the cage. If the distortive expansion of the anti-tetrahedral framework induces the increase in TEC above 400 °C, the volume of tunnels has a constant expansion rate in the whole temperature range RT to 900 °C. Contrary to what had been earlier postulated,[11] the conductivity increase above 450 °C is not correlated to a release of an extra volume in the framework's tunnels, through concerted rotation of anti-tetrahedra, which would have made the mobility of O2 and O3 ions higher than that in the Arrhenius regime at low temperature. A deeper structural analysis shows that the unconventional shift of the fully occupied O1 site above 400 °C is coupled to the distortion change and to the extra increase of the thermal vibrations of its anti-tetrahedral [$(La/Bi)_3$Mo] coordination. If the bottlenecks formed by the triangular faces of the anti-tetrahedron are little bit too narrow for an oxide ion to pass through, the spatial orientations of the spheroids of the thermal vibrations for La/Bi and Mo atoms favor the distortion/opening of the bottlenecks allowing the O1 ion to escape from its cationic tetrahedral surrounding. Then, the singular increase of the conductivity above 450 °C, fitted with the empirical VTF model, is ascribed to the framework-assisted migration of O1 oxide ions toward nearest neighboring vacancies at O2 or O3 sites. In this paper, it was also shown by using the crystallographic data reported by Tealdi et al. that, the structure of β-$La_{1.9}K_{0.1}Mo_2O_{8.9}$ is distorting upon heating the same way as the cubic bismuth-substituted $La_2Mo_2O_9$. This

behavior can probably be extrapolated to most cubic members of the LAMOX family since these derivatives exhibit, with a higher or lower magnitude depending on the nature (isovalent/aliovalent with or without a lone pair) and the amount of substitute, a concomitant increase of the TEC and of the conductivity above 400 °C. For the first time, the present study provides a clear evidence for the structural origin of the Arrhenius-VTF transition postulated in the LAMOX family of oxide ion conductors.

■ ASSOCIATED CONTENT

Supporting Information. (1) Room temperature and temperature-controlled X-ray diffraction patterns of raw powder sample of β-$La_{1.7}Bi_{0.3}Mo_2O_9$. (2) Nyquist plot of complex impedance spectrum collected on dense ceramic of β-$La_{1.7}Bi_{0.3}Mo_2O_9$ in air at 653K. (3) A comparative crystallographic model: the "linear + opening" model of thermal expansion in β-$La_{1.7}Bi_{0.3}Mo_2O_9$. (4) Distortion change of $[O1(La/K)_3Mo]$ elementary building units and of the cage as a function of temperature in β-$La_{1.9}K_{0.1}Mo_2O_{8.9}$ determined from crystallographic data published in reference [Tealdi, C.; Malavasi, L.; Ritter, C.; Flor, G.; Costa, G., *J. Solid State Chem.* **2008**, *181*, (3), 603−610.]. (5) Calculation of the volume of the trigonal bipyramid centered on O3 sites in β-$La_{1.7}Bi_{0.3}Mo_2O_9$. (6) Evolution of bond angles within the $[O1(La/Bi)_3Mo]$ anti-tetrahedral basic unit as a function of temperature in β-$La_{1.7}Bi_{0.3}Mo_2O_9$. (7) Calculation of the radius r of the sphere tangent to the three atoms forming a triangular face of the $[O1(La/Bi)_3Mo]$ anti-tetrahedron in β-$La_{1.7}Bi_{0.3}Mo_2O_9$. (8) Nearest oxygen neighbors for La/Bi atoms in β-$La_{1.7}Bi_{0.3}Mo_2O_9$. (9) Crystallographic data of β-$La_{1.7}Bi_{0.3}Mo_2O_9$ at RT, 100 °C, 200 °C, 300 °C, 400 °C, 500 °C, 600 °C, 700 °C, 800 °C, 900 °C in Crystallographic Information File (CIF) format. This material is available free of charge via the Internet at http://pubs.acs.org.

■ AUTHOR INFORMATION

Corresponding Author

*Phone: +33 (0)2 43 83 26 48. Fax: +33 (0)2 43 83 35 06. E-mail: gwenael.corbel@univ-lemans.fr.

■ REFERENCES

(1) Lacorre, P.; Goutenoire, F.; Bohnke, O.; Retoux, R.; Laligant, Y. *Nature* **2000**, *404* (6780), 856–858.
(2) Goutenoire, F.; Isnard, O.; Retoux, R.; Lacorre, P. *Chem. Mater.* **2000**, *12* (9), 2575–2580.
(3) Goutenoire, F.; Isnard, O.; Suard, E.; Bohnke, O.; Laligant, Y.; Retoux, R.; Lacorre, P. *J. Mater. Chem.* **2001**, *11* (1), 119–124.
(4) Selmi, A.; Galven, C.; Corbel, G.; Lacorre, P. *Dalton Trans.* **2010**, *39* (1), 93–102.
(5) Selmi, A.; Corbel, G.; Lacorre, P. *Solid State Ionics* **2006**, *177* (35−36), 3051–3055.
(6) Selmi, A.; Corbel, G.; Kodjikian, S.; Voronkova, V.; Kharitonova, E.; Lacorre, P. *Eur. J. Inorg. Chem.* **2008**, No. 11, 1813–1821.
(7) Corbel, G.; Durand, P.; Lacorre, P. *J. Solid State Chem.* **2009**, *182* (5), 1009–1016.
(8) Corbel, G.; Chevereau, E.; Kodjikian, S.; Lacorre, P. *Inorg. Chem.* **2007**, *46* (16), 6395–6404.
(9) Rizea, A.; Petot-Ervas, G.; Petot, C.; Abrudeanu, M.; Graham, M. J.; Sproule, G. I. *Solid State Ionics* **2007**, *177* (39−40), 3417–3424.
(10) Yashima, M.; Kakihana, M.; Yoshimura, M. *Solid State Ionics* **1996**, *86−88*, 1131–1149.
(11) Lacorre, P.; Selmi, A.; Corbel, G.; Boulard, B. *Inorg. Chem.* **2006**, *45* (2), 627–635.
(12) Vogel, H. *Phys. Z.* **1921**, *22*, 645–646.
(13) Tammann, G.; Hesse, W. *Z. Anorg. Allg. Chem.* **1926**, *156* (4), 14.
(14) Fulcher, G. S. *J. Am. Ceram. Soc.* **1925**, *8* (6), 339–355.
(15) Corbel, G.; Laligant, Y.; Goutenoire, F.; Suard, E.; Lacorre, P. *Chem. Mater.* **2005**, *17* (18), 4678–4684.
(16) Tealdi, C.; Malavasi, L.; Ritter, C.; Flor, G.; Costa, G. *J. Solid State Chem.* **2008**, *181* (3), 603–610.
(17) Lide, D. R. *CRC Handbook of Chemistry and Physics 1998−1999: A Ready-Reference Book of Chemical and Physical Data*, 79th ed.; CRC Press: Boca Raton, FL, 1998.
(18) In PDF-4 + 2009; The International Centre for Diffraction Data (ICDD), 12 Campus Boulevard, Newtown Square, Pennsylvania 19073−3273, U.S.A.
(19) Rodriguez Carvajal, J. *Phys. B* **1993**, *192* (1−2), 55–69.
(20) Berar, J. F.; Baldinozzi, G. *J. Appl. Crystallogr.* **1993**, *26*, 128–129.
(21) Fender, B. E. F. *Chemical Applications of Thermal Neutron Scattering*; Willis, B.T.M., Ed.; Oxford University Press: London, 1974.
(22) Aldebert, P.; Dianoux, A. J.; Traverse, J. P. *J. Phys. (Paris)* **1979**, *40*, 1005.
(23) Steele, D.; Fender, B. E. F. *J. Phys. C: Solid State Phys.* **1974**, *7* (1), 1–11.
(24) Martin, U.; Boysen, H.; Frey, F. *Acta Crystallogr., Sect. B: Struct. Sci.* **1993**, *49*, 403–413.
(25) Vannier, R.-N.; Abraham, F.; Nowogrocki, G.; Mairesse, G. *J. Solid State Chem.* **1999**, *142* (2), 294–304.
(26) Johnson, P. A. V.; Wright, A. C.; Sinclair, R. N. *J. Non-Cryst. Solids* **1983**, *58* (1), 109–130.
(27) Bergerhoff, G.; Berndt, M.; Brandenburg, K. *J. Res. Natl. Inst. Stand. Technol.* **1996**, *101* (3), 221–225.
(28) Johnson, D. *Z-view*, 3.0a; Scribner Associates Inc: Southern Pines, NC
(29) Georges, S.; Goutenoire, F.; Altorfer, F.; Sheptyakov, D.; Fauth, F.; Suard, E.; Lacorre, P. *Solid State Ionics* **2003**, *161* (3−4), 231–241.
(30) Hamilton, W. C. *Acta Crystallogr.* **1959**, *12* (8), 609–610.
(31) Shannon, R. D. *Acta Crystallogr.* **1976**, *A32* (5), 751–767.
(32) Andersson, S.; Åström, A. . *Proceedings of the 5th Material Research Symposium*, Gaithersburg, MD, 1971; National Bureau of Standards: Washington, DC, 1972; p 3.
(33) Angell, C. A.; Liu, C.; Sanchez, E. *Nature* **1993**, *362* (6416), 137–139.
(34) Angell, C. A.; Fan, J.; Liu, C. L.; Lu, Q.; Sanchez, E.; Xu, K. *Solid State Ionics* **1994**, *69* (3−4), 343–353.
(35) Souquet, J. L.; Levy, M.; Duclot, M. *Solid State Ionics* **1994**, *70*, 337–345.
(36) Naruke, H.; Yamase, T. *J. Solid State Chem.* **2003**, *173* (2), 407–417.
(37) Wang, X. P.; Fang, Q. F.; Li, Z. S.; Zhang, G. G.; Yi, Z. G. *Appl. Phys. Lett.* **2002**, *81* (18), 3434–3436.
(38) Fang, Q. F.; Wang, X. R.; Li, Z. S.; Zhang, G. G.; Yi, Z. G. *Mater. Sci. Eng., A* **2004**, *370* (1−2), 365–369.
(39) Jeitschko, W.; Sleight, A. W. *Acta Crystallogr.* **1972**, *B28* (11), 3174–3178.
(40) Lacorre, P. *Solid State Sci.* **2000**, *2* (8), 755–758.
(41) Mohn, C. E.; Stolen, S.; Norberg, S. T.; Hull, S. *Phys. Rev. Lett.* **2009**, *102* (15), 4.
(42) Mohn, C. E.; Stolen, S.; Norberg, S. T.; Hull, S. *Phys. Rev. B* **2009**, *80* (2), 12.
(43) Marozau, I. P.; Shaula, A. L.; Kharton, V. V.; Vyshatko, N. P.; Viskup, A. P.; Frade, J. R.; Marques, F. M. B. *Mater. Res. Bull.* **2005**, *40* (2), 361–371.